Chemical Science

EDGE ARTICLE

Check for updates

Highly efficient and very robust blue-excitable yellow phosphors built on multiple-stranded one-dimensional inorganic–organic hybrid chains†

Yang Fang,‡[a] Christopher A. Sojdak,‡[a] Gangotri Dey,[a] Simon J. Teat, [b] Mingxing Li,[c] Mircea Cotlet, [d] Kun Zhu,[a] Wei Liu,[e] Lu Wang, [a] Deirdre M. O'Carroll [f] and Jing Li [*a]

Inorganic–organic hybrid semiconductors are promising candidates for energy-related applications. Here, we have developed a unique class of multiple-stranded one-dimensional (1D) structures as very robust and efficient lighting phosphors. Following a systematic ligand design strategy, these structures are constructed by forming multiple coordination bonds between adjacent copper iodide inorganic building units Cu_mI_m (m = 2, 4, 6) (*e.g.* dimer, tetramer and hexamer clusters) and strong-binding bidentate organic ligands with low LUMO energies which give rise to infinite 1D chains of high stability and low bandgaps. The significantly enhanced thermal/photostability of these multiple-stranded chain structures is largely attributed to the multi-dentate nature and enhanced Cu–N bonding, and their excellent blue excitability is a result of using benzotriazole based ligands with low-lying LUMO energies. These facts are confirmed by Density Functional Theory (DFT) calculations. The luminescence mechanism of these compounds is studied by temperature dependent photoluminescence experiments. High internal quantum yields (IQYs) are achieved under blue excitation, marking the highest value reported so far for crystalline inorganic–organic hybrid yellow phosphors. Excellent thermal- and photo-stability, coupled with high luminescence efficiency, make this class of materials promising candidates for use as rare-earth element (REE) free phosphors in energy efficient general lighting devices.

Introduction

Inorganic–organic hybrid materials are a class of crystalline compounds composed of inorganic and organic modules that possess interesting and unique properties beyond those of their parent standalone constituents.[1–8] For example, methyl-ammonium lead halide based inorganic–organic perovskites have shown promise for the next-generation of solar devices.[9–14]

[a]Department of Chemistry and Chemical Biology, Rutgers University, 123 Bevier Road, Piscataway, NJ 08854, USA. E-mail: jingli@rutgers.edu

[b]Advanced Light Source, Lawrence Berkeley National Laboratory, 1 Cyclotron Road, Berkeley, CA 94720, USA

[c]Center for Functional Nanomaterials, Brookhaven National Laboratory, 98 Rochester Street, Upton, NY 11973, USA

[d]Center for Functional Nanomaterials, Brookhaven National Laboratory, 98 Rochester Street, Upton, NY 11973, USA

[e]Hoffman Institute of Advanced Materials, Shenzhen Polytechnic, 7098 Liuxian Blvd, Nanshan District, Shenzhen, 518055, China

[f]Department of Materials Science and Engineering, Rutgers University, 607 Taylor Road, Piscataway, NJ 08854, USA

† Electronic supplementary information (ESI) available. CCDC 1888939–1888944. For ESI and crystallographic data in CIF or other electronic format see DOI: 10.1039/c9sc00970a

‡ These authors contributed equally.

Hybrid structures with various dimensionalities have been developed, many of which exhibit interesting optical, electrical and magnetic properties.[15–19] Single crystals of one-dimensional (1D) hybrid structures have attracted enormous attention because of their large surface-to-volume ratio and defect-free nature.[20] A number of 1D hybrid materials have been explored with applications in solar cells, photodetectors and catalysis.[20–23] Recently, 1D hybrid materials have also been reported to be suitable candidates for phosphor based applications due to their highly emissive properties.[4]

One family of inorganic–organic hybrid materials of particular interest are based on I–VII binary metal halides (*e.g.* CuI). They represent one of the most promising material classes for use as low-cost, REE free lighting phosphors.[4,17,24,25] These structures range from molecular (0D) clusters to 1D chains, two-dimensional (2D) layers, and three-dimensional (3D) networks. 1D staircase-chain based hybrid structures have been studied systematically, by both experimental and theoretical methods.[4] Their optical properties, such as bandgaps and emission energies, can be deliberately tuned and modified by incorporation of organic ligands with appropriate lowest unoccupied molecular orbital (LUMO) energies. However, poor thermal stability and low internal quantum yields (IQYs) hinder their potential for real-world applications.[26,27] 1D structures built on Cu_2I_2 dimers

have been synthesized by a precursor based approach with improved IQY results but suffer from various drawbacks such as poor framework stability.[28] The thermal stability issues were addressed in 1D chain structures based on Cu_4I_4 cubane tetramers by forming strong Cu–N bonds which leads to impressively high photostability.[23] However, their main issue is the lack of blue light excitability largely attributed to the nature of the photoluminescence mechanism in such systems.

In an attempt to resolve these issues and develop highly stable, blue-light excitable yellow phosphors, we have synthesized a group of unique multiple-stranded (MS) 1D hybrid structures with specially designed ligands. All of them are based on a benzotriazole core to ensure low LUMO energies and formation of strong, multiple coordinate bonds between N and Cu.[4,24] Three 1D structures involving double- and triple-stranded chains are obtained (see Fig. 1). The individual inorganic modules are dimers, tetramers, and hexamers, respectively, in these structures. The targeted hybrid compounds have a high IQY (>70%) under blue-light excitation, as well as exceptional thermal- and photo-stability. In addition, their band gaps and optical properties can be systematically and fine-tuned by incorporating ligands of suitable LUMO energies.

Experimental section

Materials

CuI (98%, Alfa Aesar), bulk methanol (98%, Alfa Aesar), dichloromethane (99+%, Alfa Aesar), benzotriazole (99%, Alfa Aesar), benzimidazole (99%, Alfa Aesar), 2-methyl-1H-imidazole (99%, Alfa Aesar), 1,5-dibromopentane (99%, Alfa Aesar), 1,4-dibromobutane (99%, Alfa Aesar), 1-chloro-3-bromopropane (>98%, Alfa Aesar), 3-bromopyridine (99%, Alfa Aesar), 1,4-bis(bromomethyl)benzene (99%, Alfa Aesar), ethylene glycol (99%, Alfa Aesar), potassium carbonate (99%, Alfa Aesar), copper chloride (99%, Alfa Aesar), sodium salicylate (99%, Merck), $BaMgAl_{10}O_{17}:Eu^{2+}$ and $YAG:Ce^{3+}$ type 9800 (Global Tungsten & Powders Corp), and PolyOx N750 (Dow Chemical).

Preparation of 1,5-bis(1H-benzo[d][1,2,3]triazol-1-yl)pentane (bbtpe). Benzotriazole (20 mmol) was first dissolved in DMSO (30 ml), and then NaOH (20 mmol) and 1,5-dibromopentane (10 mmol) were added. The solution was stirred at 80 °C overnight, and the reaction solution was poured into ice water to form a white precipitate. The crude product was collected by filtration and purified through column chromatography with ethyl acetate and hexane as solvent. The yield was 45%.

Preparation of 1,4-bis(1H-benzo[d][1,2,3]triazol-1-yl)butane (bbtbu). The synthesis of bbtbu was carried out by a modified version of the reported method. Benzotriazole (20 mmol) was added to DMSO (20 ml) containing NaOH (20 mmol). Then 1,4-dibromobutane was added and the reaction solution was stirred at 80 °C overnight. The reaction solution was poured into ice water to form a white precipitate. After collecting the crude product through filtration, acetone (30 ml) was used to completely dissolve the white precipitate. $CuCl_2$ saturated solution in acetone was added into the previous resulting solution dropwise, until there was no more green precipitate formed. The green precipitate was filtered out again and washed with cold ethanol. Then DMSO (10 ml) was used to dissolve the obtained green precipitate, and the obtained solution was poured into ice water (100 ml). A pure product bbtbu was formed as a white precipitate in water. The pure bbtbu product was collected through filtration and dried under vacuum. The yield was 43%.

Preparation of 1,4-bis(2-methyl-1H-imidazol-1-yl)butane (bmibu). 2-Methyl-1H-imidazole (10 mmol) was first dissolved in DMSO (20 ml), and then NaOH (20 mmol) and 1,4-dibromobutane (10 mmol) were added. After heating the reaction solution in an 80 °C oil bath for 10 h, the reaction solution was poured into ice water to form a white precipitate. The product was further purified through recrystallization with ethanol. A white crystal was obtained. The yield was 93%.

Preparation of 1-(3-chloropropyl)-1H-benzo[d][1,2,3]triazole (3-Cl-pr-bt). Benzotriazole (10 mmol) and 1-chloro-3-bromopropane (10 mmol) were dissolved in 40 ml CH_3CN. Then K_2CO_3 (20 mmol) was added into the solution, and the
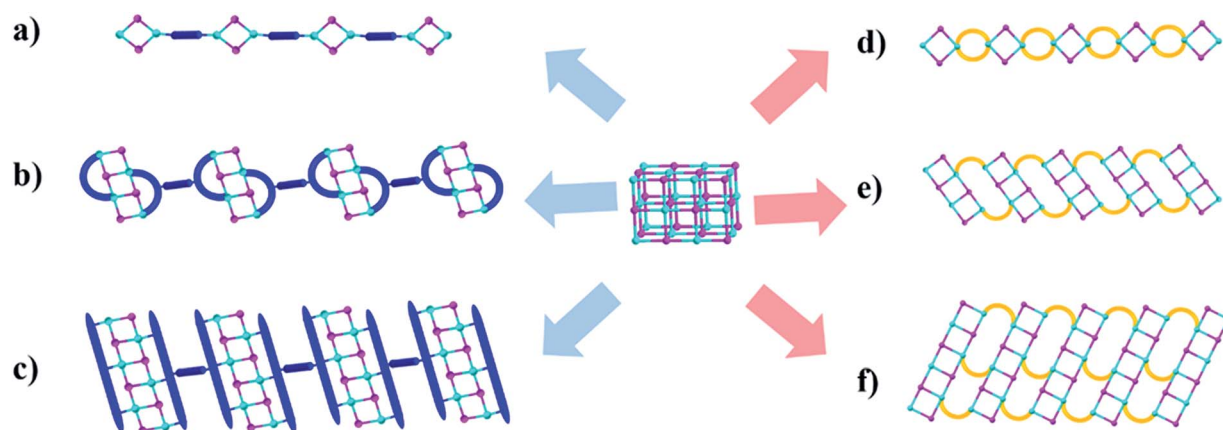

Fig. 1 Schematic illustrating the design and construction of 1D multiple-stranded hybrid structures: (a) 1D single-stranded structure based on the Cu_2I_2 dimer. (b) 1D single-stranded structure based on the Cu_4I_4 tetramer. (c) 1D single-stranded structure based on the Cu_6I_6 hexamer. (d) 1D double-stranded structure based on the Cu_2I_2 dimer. (e) 1D double-stranded structure based on the Cu_4I_4 tetramer. (f) 1D triple-stranded structure based on the Cu_6I_6 hexamer. Color scheme of the balls: cyan: Cu, pink: I, and orange and blue rods: organic ligands.

solution was stirred at room temperature for two days. The reaction solution was filtered, concentrated and purified *via* column chromatography with ethyl acetate and hexane. A colorless oil product was collected. The yield was 50%.

Preparation of 1-(3-(1*H*-benzo[*d*]imidazol-1-yl)propyl)-1*H*-benzo[*d*][1,2,3]triazole (biprbt). 3-Cl-pr-bt (5 mmol) and benzimidazole (5 mmol) were dissolved in DMSO (20 ml). Then NaOH (10 mmol) was added. The reaction solution was kept in an 80 °C oil bath for one day. After cooling the reaction solution, the solution was poured into 150 ml of ice water and a white precipitate was formed. The precipitate was collected *via* filtration, washed with hexane and dried under vacuum. The yield was 95%.

Preparation of 1-(6-(1*H*-benzo[*d*]imidazol-1-yl)hexyl)-1*H*-benzo[*d*][1,2,3]triazole (bihebt). The preparation of bihebt is similar to that of biprbt. The yield is 93%.

Synthesis of 1D-Cu$_2$I$_2$(biprbt)$_2$ (1). Acetonitrile (2 ml) was added into KI saturated solution (2 ml) containing CuI (1 mmol), and then biprbt (0.5 mmol) in methanol (2 ml) was slowly added. Yellow-green cube-shaped crystals were obtained after CuI (1 mmol) and biprbt (1 mmol) layers diffused for two days. The yield was 73%.

Synthesis of 1D-Cu$_2$I$_2$(bbtbu)$_2$ (2). Compound **2** was prepared similarly to **1** except for the ligand. Yellow rod-shaped crystals were obtained after CuI (1 mmol) and bbtbu (1 mmol) layers diffused for two days. The yield was 76%.

Synthesis of 1D-Cu$_2$I$_2$(bihebt)$_2$ (3). Compound **3** was prepared similarly to **1** except for the ligand. Yellow plate-shaped single crystals were obtained after CuI (1 mmol) and bihebt (1 mmol) layers diffused for three days. The yield was 70%.

Synthesis of 1D-Cu$_2$I$_2$(bbtpe)$_2$ (4). Compound **4** was prepared similarly to **1** except for the ligand. Yellow-green plate-shaped single crystals were obtained after CuI (1 mmol) and bbtpe (1 mmol) layers diffused for one day. The yield was 76%.

Synthesis of 1D-Cu$_4$I$_4$(bbtpe)$_2$ (5). CuI (1 mmol) and bbtpe (0.5 mmol) was sealed in a Pyrex tube with CH$_3$CN (4 ml) as the solvent. The reaction tube was heated in a 120 °C oven for two days. Yellow cubic-shaped single crystals were formed and were collected by filtration. The yield was 74%.

Synthesis of 1D-Cu$_6$I$_6$(bmibu)$_3$ (6). Compound **6** was prepared similarly to **1** except for the ligand. Transparent cube-shaped crystals of **6** were obtained after CuI (1 mmol) and bmibu (1 mmol) layers diffused for three days. The yield was 84%.

Single crystal X-ray diffraction (SCXRD). Single crystal data of **1–5** were collected on a D8 goniostat equipped with a Bruker PHOTONII CPAD detector, while those of **6** were collected with a Bruker PHOTON100 CMOS detector, at the Advanced Light Source (ALS), Lawrence Berkeley National Laboratory, using synchrotron radiation. The structures were solved by direct methods and refined by full-matrix least-squares on F2 using the Bruker SHELXTL package. These data can be obtained free of charge from The Cambridge Crystallographic Data Centre *via* www.ccdc.cam.ac.uk/data_request/cif. The structures were deposited in the Cambridge Structural Database (CSD) with numbers: 1888939–1888944.

Powder X-ray diffraction (PXRD) analysis. Powder X-ray diffraction (PXRD) analyses were carried out on a Rigaku Ultima-IV unit using Cu Kα radiation (λ = 1.5406 Å). The data were collected at room temperature in a 2θ range of 5°–40° with a scan speed of 2° min^{-1}. The operating power was 40 kV/40 mA.

Room-temperature photoluminescence measurements. PL measurements were carried out on a Varian Cary Eclipse spectrophotometer. Powder samples were evenly distributed and sandwiched between two glass slides (which do not have emission in the visible range) for room temperature measurements.

Temperature dependent photoluminescence spectroscopy and lifetime measurements. Pressed pellets of 1 to 1.5 mm thickness were prepared in a 10 mm diameter die with a pressure of approximately 3000 psi. Temperature dependent PL spectra and time-resolved PL decays were recorded with a home built time-correlated single photon counting instrument consisting of a 380 nm frequency doubled femtosecond solid state laser system as the excitation source (Maitai, Spectra Physics, 100 fs pulse, 10 kHz repetition rate), a Janis cryostat model V500, and an optical detection system comprised of a single photon counting avalanche photodiode (PMD50, PicoQuant Germany, 250 ps response time), a time analyzer (TimeHarp 260 nano, PicoQuant Germany) and an Ocean Optics FL65000 fiber optics spectrometer. The PL signal emitted by the sample was collected by a 50 mm biconvex lens and split by a 50/50 non-polarizing beam splitter cube between the photodiode and spectrometer. PL signals were acquired using an average power of 0.55 mW, with decays recorded in at least 1000 channels using either a 550 nm/88 nm bandpass filter (Thorlabs) or a 750 nm longpass filter (Thorlabs). Decays were individually fit with FluoFit PicoQuant software using a biexponential fitting model.

Thermogravimetric analysis. Thermogravimetric analyses (TGA) of samples were performed using a TA Instrument Q5000IR thermal gravimetric analyzer with a nitrogen flow and sample purge rate of 10 ml min^{-1} and 12 ml min^{-1} respectively. About 3 mg of samples were loaded onto a platinum sample pan and heated from room temperature to 450 °C at a rate of 10 °C min^{-1} under a nitrogen flow.

Diffuse reflectance spectroscopy. Optical absorption spectra were measured at room temperature on a Shimadzu UV-3600 UV/VIS/NIR spectrometer. The reflectance data were converted to the Kubelka–Munk function, $\alpha/S = (1 - R)^2/2R$ (α is the absorption coefficient, S is the scattering coefficient and R is the reflectance), and used to estimate the bandgap. The scattering coefficient (S) was treated as a constant as the average particle size of the samples used in the measurements was significantly larger than 5 μm. Samples for reflectance measurements were prepared by evenly distributing ground powder samples between two quartz slides.

Internal and external quantum yield measurements. Internal quantum yield (IQY) measurements were made on a C9920-02 absolute quantum yield measurement system (Hamamatsu Photonics) with a 150 W xenon monochromatic light source and 3.3 inch integrating sphere. Samples for internal quantum yield measurements were prepared by

spreading fine powder samples evenly on the bottom of a quartz sample holder. Sodium salicylate (SS) and YAG:Ce^{3+} were chosen as the standards with reported IQY values of 60% and 95% at an excitation energy of 360 nm and 450 nm, respectively.[29,30] Their IQY values were measured to be 66% and 97%, respectively and corrections were made based on the reported data. The external quantum yields (EQY) of these samples were estimated from their IQY and reflectance R using the equation EQY = IQY × (1 − R), where R is the portion of photons reflected.[31] BaMgAl$_{10}$O$_{17}$:Eu^{2+} and YAG:Ce^{3+} were chosen as the standards with reported EQY values of 70% and 90% at an excitation energy of 360 nm and 450 nm, respectively.[32]

DFT calculations. DFT calculations were carried out for selected 1D-Cu$_m$I$_m$(L)$_y$ compounds using the Quantum Espresso software package.[33] We have used the PBE functional[34] for their geometry optimization and the PBE0 hybrid functional for the band gap calculation of 1D-Cu$_2$I$_2$(bbtpe)$_2$ (**4**).[35] This is because the GGA functionals underestimate the band gaps of materials.[36] In all calculations, norm-conserving pseudopotentials[37] and a plane wave basis were used with a kinetic energy cutoff of 60 Ry. Our previous calculations showed that increasing the kinetic energy cutoff by 2 to 3 times does not change the band gap of similar hybrid materials by more than 0.01 eV.[25] The Brillouin zone of each crystal was sampled using Γ-centered k-points with a Gaussian broadening of 0.005 Ry. For the geometry optimization, the initial structures of the hybrid compounds were taken from experimental data. A quasi-Newton algorithm with a convergence threshold of 10^{-3} Ry per Bohr was used to relax the geometry. To calculate the binding energies, E_b, between Cu and ligands, we used clusters containing a Cu$_2$I$_2$ core and four coordinating ligands. Geometry optimization was performed for the cluster and the ligands, respectively. Due to the instability of the Cu$_2$I$_2$ core, its energy is reported as the single-point energy using the experimental geometry. For Cu$_2$I$_2$(bbtpe)$_4$, the binding energy was computed as $E_b = \dfrac{E(Cu_2I_2L_4) - 4E(L) - E(Cu_2I_2)}{4}$, where L represent a ligand. $E(Cu_2I_2L_4)$, $E(L)$ and $E(Cu_2I_2)$ are the energies of the compound, the ligand and the Cu$_2$I$_2$ core, respectively, in the gas phase. For Cu$_2$I$_2$(tpp)$_2$(pz)$_2$ and Cu$_2$I$_2$(tpp)$_2$(4,4′-bpy)$_2$,

$$E_b = \frac{E(Cu_2I_2L_4) - 2E(L) - 2E(tpp) - E(Cu_2I_2)}{2} - E_b(Cu-P).$$

Here E_b(Cu–P) represents the binding energy between Cu and the P atom in the compound Cu$_2$I$_2$(tpp)$_3$, and

$$E_b(Cu-P) = \frac{E(Cu_2I_2(tpp)_3) - 3E(tpp) - E(Cu_2I_2)}{3}.$$

Fabrication of prototype LED bulbs. Selected phosphors were dispersed in binder/ethanol solution, and were uniformly coated onto glass bulbs. The bulbs were placed on top of LED lamps with UV chips (110 V, 2 W, and 450 nm) as the excitation source.

Results and discussion

Design strategy

Our early studies have shown that among copper iodide based hybrid compounds those built from Cu$_m$I$_m$ molecular clusters

(*e.g. m* = 2–6) are much more efficient light emitters than those made of (CuI)$_∞$ modules (*e.g.* infinite chains or layers). However, the molecular structures suffer from low thermal, moisture and photostability. To tackle such a problem we have designed a series of multiple-stranded structures (Fig. 1d–f). They can be regarded as one-dimensional (1D) chains built by connecting the neighboring molecular Cu$_m$I$_m$ (*m* = 2, 4 and 6) building units through multiple organic ligands. Such a multiple-stranded bonding mode greatly enhances their framework stability over single-stranded structures, where the inorganic molecular motifs are interconnected by a single ligand (Fig. 1a–c). We have achieved double- and triple-stranded structures by designing a series of flexible benzotriazole and imidazole derivatives that contain at least three carbon atoms in the alkyl chains between two binding sites (*N*) (Fig. S1, ESI†), as shorter alkyl chains tend to produce single-stranded structures. Our hypothesis is that multiple-stranded structures constructed from low LUMO energy ligands and highly emissive Cu$_m$I$_m$ molecular motifs will form stronger bonds between inorganic motifs and organic ligands and will produce robust compounds with strong blue excitability and high PL efficiency.

By a slow diffusion approach we have synthesized six new multiple-stranded compounds: 1D-Cu$_2$I$_2$(biprbt)$_2$ (**1**) (biprbt = 1-(3-(1*H*-benzo[*d*]imidazol-1-yl)propyl)-1*H*-benzo[*d*][1,2,3]triazole), 1D-Cu$_2$I$_2$(bbtbu)$_2$ (**2**) (bbtbu = 1,4-bis(1*H*-benzo[*d*][1,2,3]triazol-1-yl)butane), 1D-Cu$_2$I$_2$(bihebt)$_2$ (**3**) (bihebt = 1-(6-(1*H*-benzo[*d*]imidazol-1-yl)hexyl)-1*H*-benzo[*d*][1,2,3]triazole), 1D-Cu$_2$I$_2$(bbtpe)$_2$ (**4**) (bbtpe = 1,5-bis(1*H*-benzo[*d*][1,2,3]triazol-1-yl)pentane), 1D-Cu$_4$I$_4$(bbtpe)$_2$ (**5**), and 1D-Cu$_6$I$_6$(bmibu)$_3$ (**6**) (bmibu = 1,4-bis(2-methyl-1*H*-imidazol-1-yl)butane). For example, use of CuI and the organic ligand bbtpe through interlayer diffusion at room temperature results in a Cu$_2$I$_2$ dimer based structure 1D-Cu$_2$I$_2$(bbtpe)$_2$ (**4**), while heating CuI and bbtpe in a Pyrex tube at 120 °C led to the formation of a Cu$_4$I$_4$ staircase tetramer based structure 1D-Cu$_4$I$_4$(bbtpe)$_2$ (**5**). Further experimental details for the synthesis of other compounds can be found in the ESI† (Experimental section, Fig. S7–S12, ESI†). The phase purity of the products was confirmed by powder X-ray diffraction (PXRD) analysis (Fig. S16 and S17, ESI†).

Structure description

Crystal structure analysis reveals the formation of 1D structures composed of an inorganic rhomboid dimer, staircase tetramer or hexamer bonded by multiple organic linkers (Fig. 2). Single crystal data of the six compounds are summarized in Table 1. All but compound **2** crystallize in the $P\bar{1}$ space group, while the latter crystalizes in the $P\bar{4}2c$ space group. Compounds **1–4** have the general formula 1D-Cu$_2$I$_2$(L)$_2$ where each copper metal is tetrahedrally coordinated to two nitrogen atoms from two ligands and to two iodine atoms (Fig. 2a, S13–S15, ESI†). Each Cu$_2$I$_2$ inorganic motif is interconnected by four bidentate ligands to form a new type of 1D double-stranded chain structure. Different from previously reported 1D single-stranded structures based on the same Cu$_2$I$_2$ module (Fig. 1a), here two ligands coordinate to the same Cu atom. While Cu–Cu distances in compounds **1** and **4** are longer than the sum of van
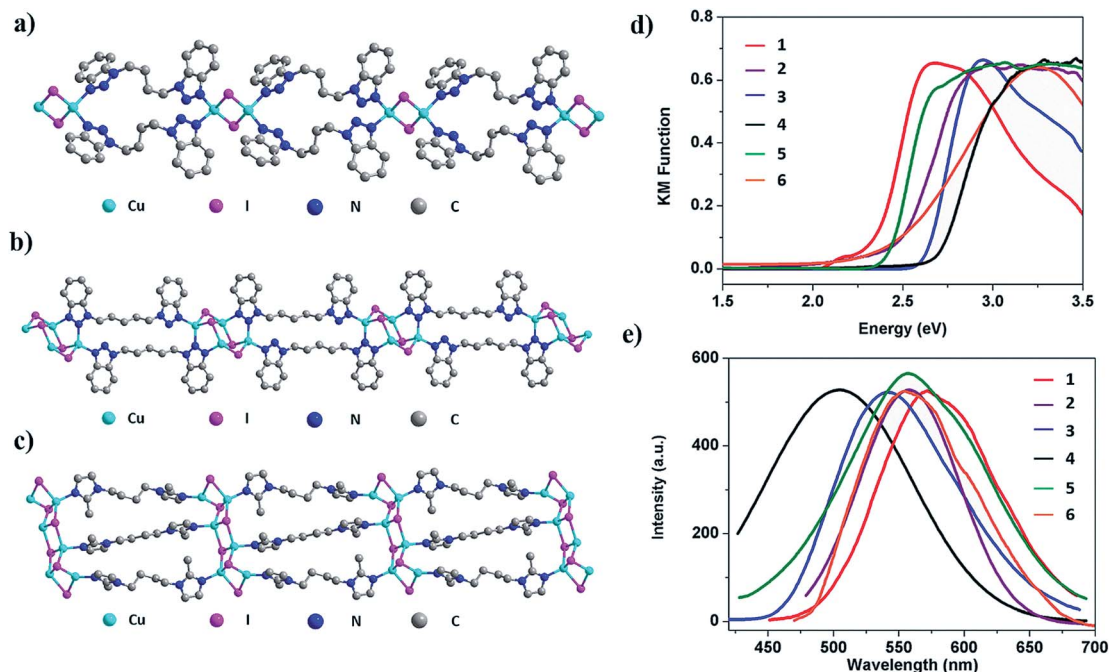
Fig. 2 (a) 1D-Cu_2I_2(bbtbu)$_2$ (**2**). (b) 1D-Cu_4I_4(bbtpe)$_2$ (**5**). (c) 1D-Cu_6I_6(bmibu)$_3$ (**6**). Color scheme of the atoms: Cu: cyan, I: pink, N: blue, and C: grey. (d) Optical absorption spectra of **1** (red), **2** (purple), **3** (blue), **4** (black), **5** (olive), and **6** (orange). (e) Photoluminescence spectra ($\lambda_{ex} = 360$ nm) of **1** (red), **2** (purple), **3** (blue), **4** (black), **5** (olive), and **6** (orange).

der Waals radii of Cu atoms (2.8 Å), similar to those found in single-stranded 1D structures containing the same dimer unit, the values are much shorter in compounds **2** and **3** (Table S1, ESI†). In compound **5** the ligand bbtpe coordinates to the staircase-like Cu_4I_4 tetramer *via* a bidentate/monodentate binding mode of the benzotriazole moiety. The asymmetric unit of compound **5** contains two crystallographically independent Cu centers, two I$^-$ and two bbtpe ligands (Fig. 2b). One Cu center is coordinated to two N donors from two different bbtpe ligands, one μ$_2$-I and one μ$_3$-I bridges, forming a [CuN$_2$I$_2$]

tetrahedron. The other Cu center is coordinated to one N atom, one μ$_2$-I and two μ$_3$-I, forming a CuNI$_3$ tetrahedron. The Cu–Cu distances in **5** are 2.6133(9) and 2.7796(6) Å. Similar to double-stranded 1D compounds based on dimers (**1–4**), compound **5** has a double-stranded 1D structure composed of a Cu_4I_4 tetramer. The structure of compound **6** is built from a Cu_6I_6 staircase hexamer and accompanying bidentate ligands with a formula of 1D-Cu_6I_6(bmibu)$_3$ (Fig. 2c). There is a crystallographic center of inversion located at the middle of Cu_6I_6 unit. Each bmibu ligand in compound **6** binds to two Cu atoms from

Table 1 Summary of crystal data of compounds **1–6**

Compound	1D-Cu_2I_2(biprbt)$_2$ (**1**)	1D-Cu_2I_2(bbtbu)$_2$ (**2**)	1D-Cu_2I_2(bihebt)$_2$ (**3**)	1D-Cu_2I_2(bbtpe)$_2$ (**4**)	1D-Cu_4I_4(bbtpe)$_2$ (**5**)	1D-Cu_6I_6(bmibu)$_3$ (**6**)
Empirical formula	$C_{16}H_{15}CuIN_5$	$C_{16}H_{16}CuIN_6$	$C_{19}H_{21}CuIN_5$	$C_{17}H_{18}CuIN_6$	$C_{17}H_{18}Cu_2I_2N_6$	$C_{18}H_{27}Cu_3I_3N_6$
FW	467.77	482.79	509.85	496.81	687.25	898.77
Space group	$P\bar{1}$	$P\bar{4}2c$	$P\bar{1}$	$P\bar{1}$	$P\bar{1}$	$P\bar{1}$
a (Å)	8.5197(3)	13.8410(8)	9.4723(9)	9.3371(5)	8.3419(5)	10.2612(5)
b (Å)	9.4963(3)	13.8410(8)	10.8047(10)	10.3738(6)	10.1955(6)	10.7326(6)
c (Å)	10.5529(4)	8.7594(6)	10.9194(11)	10.4214(6)	13.6890(8)	11.8422(7)
α (°)	85.8689(12)	90	69.009(3)	82.819(2)	76.369(2)	106.811(3)
β (°)	77.7990(12)	90	64.607(3)	81.825(2)	74.522(2)	90.123(3)
γ (°)	71.5887(12)	90	80.659(3)	63.474(2)	66.570(2)	101.770(3)
V (Å^3)	791.78(5)	1678.1(2)	942.53(16)	891.83(9)	1018.40(11)	1219.58(12)
Z	2	4	2	2	2	2
T (K)	100 (2)	100(2)	100 (2)	100 (2)	100 (2)	100 (2)
λ (Å)	0.7288	0.7749	0.7288	0.7293	0.7749	0.7749
R_1	0.0257	0.0484	0.0367	0.0359	0.0502	0.0406
wR_2	0.0483	0.1091	0.0674	0.0741	0.0755	0.0602

two neighboring Cu_6I_6 units. Similarly, two types of Cu atoms are found in the Cu_6I_6 unit, one of which is coordinated to one N atom from the bmibu ligand, one μ_2-I, and one μ_3-I atom. The other Cu center is coordinated to one N, one μ_2-I and two μ_3-I. Although a few Cu_6I_6 hexamer based structures have been reported prior to this work, this 1D triple-stranded structure is unprecedented.[38,39] Cu–Cu distances in compound **6** are longer and shorter compared to the sum of van der Waals radii of Cu atoms (Table S1, ESI†).

Optical properties, luminescence efficiency and emission mechanism

The photophysical properties of the multiple-stranded 1D structures were first investigated at room temperature. Optical absorption spectra and room temperature solid state photo-luminescence (PL) data of compounds **1–6** are plotted in Fig. 2d and e. The estimated band gap values as well as emission properties are summarized in Table 2. The absorption spectra feature sharp slopes, characteristic of efficient light absorption of these materials. The estimated band gaps range from 2.3 to 2.7 eV. For $1D\text{-}Cu_2I_2(bbtpe)_2$ (**4**), a value of 2.62 eV was estimated from DFT calculations (see DFT calculations in the Experimental section), which is in good agreement with its optical band gap of ∼2.7 eV. Similar to the trend observed in 1D-CuI(L) staircase-like chain structures[4] and benzotriazole derivative based CuI AIO structures,[25] larger band gap values correspond to higher energy emission. For example, with the largest experimental band gap of 2.7 eV, compound **4** emits at 508 nm, which is the highest emission energy among all six compounds. The emission spectra of all 1D structures are characteristic of a broad single band, and their emission maximum is in the green-orange region of the visible light spectrum. The room temperature internal quantum yields (IQYs) are estimated at two excitation energies and the results are also shown in Table 2. The values range from 56% to 83% and from 20 to 70% under 365 and 450 nm excitation, respectively. The highest values are reported for $1D\text{-}Cu_4I_4(bbtpe)_2$ (**5**), 83% (λ_{ex} = 365 nm) and 70% (λ_{ex} = 450 nm), which correlate well with its excitation spectrum (Fig. S27, ESI†). To the best of our knowledge, the latter is among the highest values achieved to date for any crystalline hybrid phosphors under blue-light excitation.[28]

Temperature dependent PL experiments were then carried out on selected compounds. For compound **5**, lowering temperature results in a significant increase in luminescence

intensity. This behaviour could be explained by increased localization of the excited state on the molecular structure and reduced structural torsion, which acts to increase the luminescence efficiency.[40,41] Besides the observed intensity changes, the shape and wavelength of the emission spectrum do not change significantly with temperature (Fig. 5a and S26†).

Luminescence decay measurements were also conducted on selected compounds, namely **1** and **5** (Fig. 5b and S26, Tables S3 and S4, ESI†). The long average lifetimes (∼6.6 μs and 2.3 μs, respectively) of the two compounds at room temperature (293 K or 20 °C) suggest that emission proceeds primarily from a triplet excited electronic state. Compound **5** has a shorter average lifetime than compound **1** at higher temperatures. This is consistent with the higher room-temperature IQY of **5** (Table 2), as a shorter lifetime is generally consistent with more efficient recombination. Both compounds exhibit a shortening of their average luminescence lifetime with increasing temperature (between 77 and 293 K). Given the observed reduction in luminescence intensity that also occurs with increasing temperature (Fig. 5a), the short lifetime at room temperature may be attributed to non-radiative decay rate enhancement possibly due to increased structural torsion. However, this is at odds with the high IQY of **5** at room temperature (>70%). It is possible that the IQY of compound **5** is even higher at low temperatures compared to its room-temperature value, due to more efficient long-lived phosphorescence.

The luminescence decay curves were best fit with bi-exponential decay functions, suggesting two different recombination pathways, one with a decay time of tens of μs and the other with a decay time of a few μs. Both the long and short decay components decreased with increasing temperature; however, their relative contributions to the average lifetime varied significantly. Compound **1** retains a relatively high percentage of the longer lifetime decay component with increasing temperature (*e.g.*, ∼67% of the longer ∼9 μs component and only 33% of the shorter ∼2 μs component at 293 K), whereas compound **5** has a significant increase in the shorter lifetime decay component with increasing temperature (only 29% of the longer 4 μs component and 71% of the shorter ∼1 μs component at 293 K). This significant change in the contributions of short and long lifetime components with increasing temperature indicates that there is a thermally activated recombination pathway. A new defect pathway activated at higher temperature or a reduction in the efficiency of metal-to-ligand or halide-to-

Table 2 Estimated optical band gaps, emission energies and colors, IQY values and decomposition temperatures of compounds **1–6**

#	Structure	Optical bandgap (eV)	λ_{em} (nm)	Emission color	IQY (EQY) (λ_{ex}: 360 nm)	IQY (EQY) (λ_{ex}: 450 nm)	T_D (°C)
1	$1D\text{-}Cu_2I_2(biprbt)_2$	2.3	572	Yellow	56 (39)	20 (15)	260
2	$1D\text{-}Cu_2I_2(bbtbu)_2$	2.4	562	Yellow	66 (44)	31 (23)	250
3	$1D\text{-}Cu_2I_2(bihebt)_2$	2.6	542	Yellow	63 (45)	22 (16)	250
4	$1D\text{-}Cu_2I_2(bbtpe)_2$	2.7	508	Blue-green	83 (57)	35 (26)	250
5	$1D\text{-}Cu_4I_4(bbtpe)_2$	2.4	560	Yellow	82 (49)	70 (40)	250
6	$1D\text{-}Cu_6I_6(bmibu)_3$	2.5	554	Yellow	50 (38)	34 (19)	280

ligand charge transfer with increasing temperature could lead to this type of strong temperature-dependent luminescence behavior. However, given the high IQY of **5**, it is also possible that the excited state decays radiatively throughout two channels, one being phosphorescence (characterized by the long decay components (tens of μs)) and the other being a less-efficient thermally activated delayed fluorescence channel (short, μs decay component). The latter can occur when the singlet and triplet states are energetically close, which in turn enables backwards (reverse) intersystem crossing and radiative decay *via* delayed fluorescence.

Band structure calculations

Band structure (BS) and density of states (DOS) calculations were performed on selected structures employing DFT methods using the CASTEP package[42] (S7, ESI†). The calculated density of states (DOS) are shown in Fig. 3 and in the ESI (Fig. S20–S25†). The contribution to the valence band maximum (VBM) primarily originates from the inorganic components (*e.g.* Cu 3d and I 5p), while the conduction band minimum (CBM) is composed primarily of the atomic states that make up the LUMOs of organic ligands, specifically C 2p and N 2p orbitals. This composition is similar to the results found in a number of other types of copper iodide based hybrid structures, including 1D-CuI(L)[4] and nD-Cu$_2$I$_2$(L$_m$) (n = 0–2) structures.[28,43] Therefore, the band gap of multiple-stranded structures can also be systematically tuned by incorporating organic ligands with relatively low LUMO energies to achieve desired low band gaps and low energy emission wavelengths. For example, compounds **1-4** are all double-stranded dimers, and their experimental band gaps are estimated to be 2.3, 2.4, 2.6 and 2.7 eV, respectively, correlating with their increasing LUMO energy of the corresponding ligands, −1.661, −1.621, −1.565, and −1.563 eV (S9, ESI†).

Thermal- and photo-stability

The significantly improved thermal stability of these 1D structures was evaluated by TG analysis (Fig. S18, ESI†). TGA curves show that there is only one major weight loss stage for **1–6** and all compounds demonstrate stability up to 250 °C (Table 2). Compared to previously reported stability data of 1D-CuI(L) and nD-Cu$_2$I$_2$(L$_m$) (n = 0–2), compounds **1–6** have significantly

higher thermal stability. For example, the double-stranded structure 1D-Cu$_2$I$_2$(bbtpe)$_2$ is stable up to 250 °C, while the single-stranded chain structures 1D-Cu$_2$I$_2$(tpp)$_2$(pz) (tpp = triphenylphosphine, pz = pyrazine) and 1D-Cu$_2$I$_2$(tpp)$_2$(4,4′-bpy) (4,4′-bpy = bipyridine) readily undergo thermal decomposition at 120 and 160 °C (Fig. S28 and S29, ESI†).[28]

To quantitatively assess Cu–N binding energies in these compounds, DFT calculations[33] were performed to compare the Cu–N bonding strength in compound **4** with those of the two single-stranded structures made of Cu$_2$I$_2$ dimers, namely 1D-Cu$_2$I$_2$(tpp)$_2$(pz) and 1D-Cu$_2$I$_2$(tpp)$_2$(4,4′-bpy) (see DFT calculations in the Experimental section). As illustrated in Fig. 4, the Cu–N binding energies, E_b, are 1.60, 1.36, and 1.29 eV for the ligands bbtpe, pz and 4,4′-bpy, respectively. These values indicate that the increased stability of compound **4** compared to single-stranded 1D structures arises from the stronger bonding interactions between the metal ion and the ligand nitrogen. In addition, in double-stranded structures such as compound **4**, the neighboring Cu$_2$I$_2$ cores are connected through two ligands, whereas in single-stranded structures such as 1D-Cu$_2$I$_2$(tpp)$_2$(pz) and 1D-Cu$_2$I$_2$(tpp)$_2$(4,4′-bpy), they are linked by only one ligand. As a result, the double-stranded connections are more robust than single-stranded connections. Furthermore, in the crystal structure of compound **4**, the neighboring aromatic
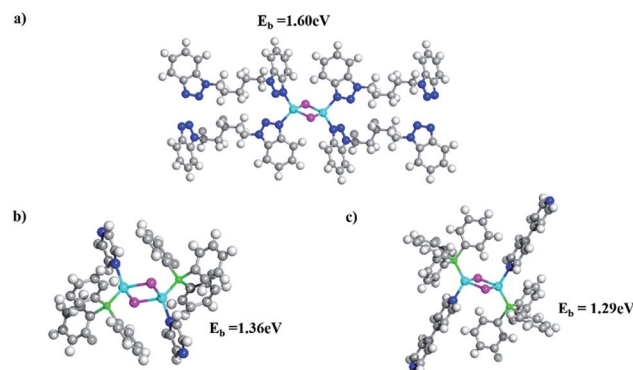

Fig. 4 Optimized structures of (a) Cu$_2$I$_2$(bbtpe)$_4$, (b) Cu$_2$I$_2$(tpp)$_2$(pz)$_2$, and (c) Cu$_2$I$_2$(tpp)$_2$(4,4′-bpy)$_2$. Cu, I, N, C, O, P, and H atoms are shown in cyan, purple, blue, gray, red, green and white, respectively. The binding energy (E_b) value is indicated for each complex.
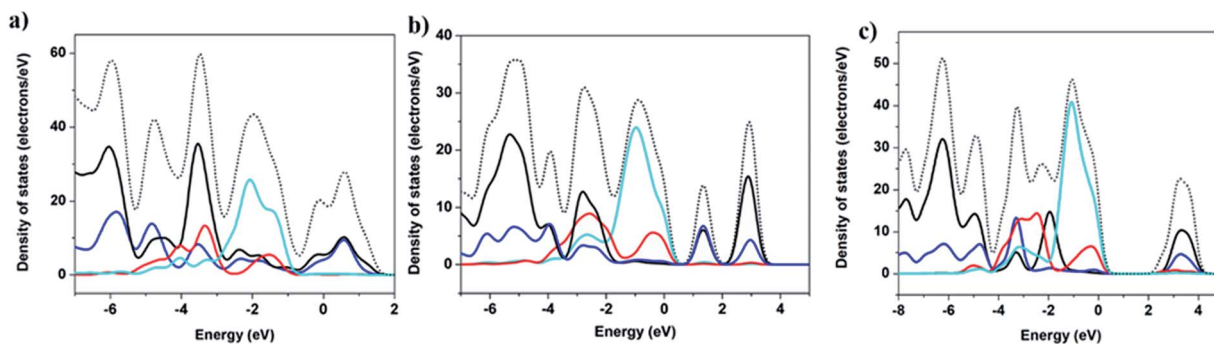

Fig. 3 Calculated density of states (DOS): (a) 1D-Cu$_2$I$_2$(biprbt)$_2$. (b) 1D-Cu$_4$I$_4$(bbtpe)$_2$. (c) 1D-Cu$_6$I$_6$(bmibu)$_3$. Color scheme: total DOS (dashed black), Cu 3d orbitals (cyan), I 5p orbitals (red), N 2p orbitals (blue), and C 2p orbitals (black).
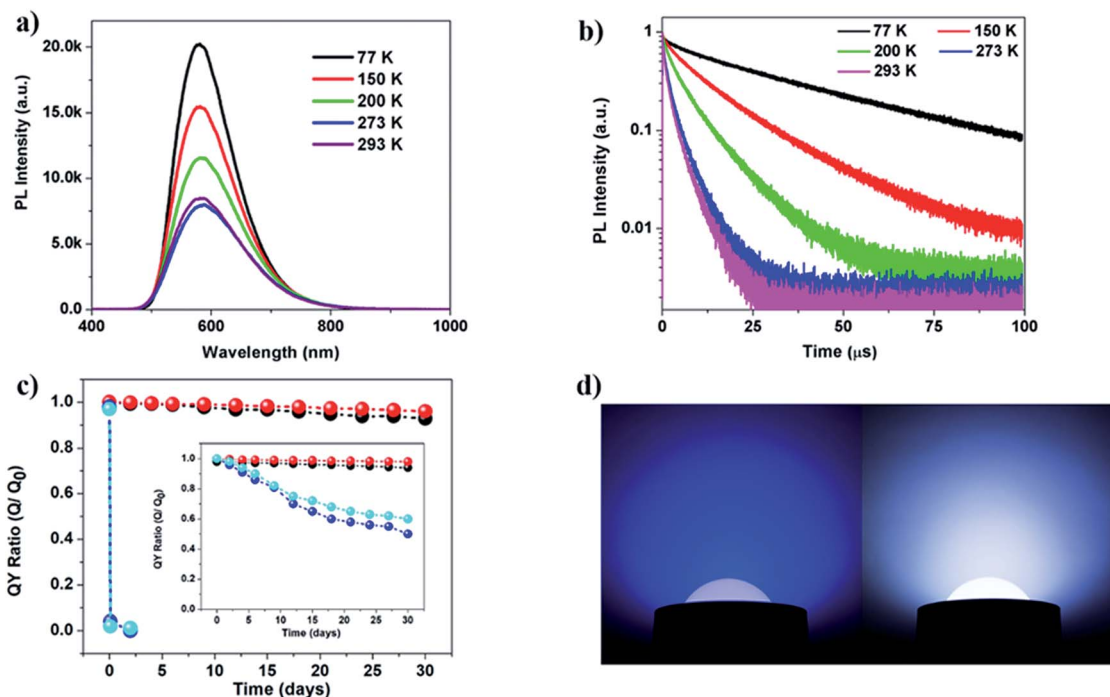
Fig. 5 (a) Emission spectra and (b) luminescence decay profiles of compound **5** at various temperatures ($\lambda_{ex} = 480$ nm). (c) Plots of IQY ratios (Q_0 and Q are IQY values measured before and after heating the sample at 150 °C in air as a function of time). Inset is the plot of ratios of the IQY values after and before exposing to UV light as a function of time for 30 days. Blue: 0D-$Cu_2I_2(py)_4$, cyan: 1D-$Cu_2I_2(tpp)_2(pz)$, black: compound **1**, and red: compound **5**. (d) Prototype illuminating bulbs made of a blue LED chip (left) and compound **5** coated blue LED chip (right).

ligands bbtpe are oriented almost parallel to each other, thus enhancing the π–π interactions in the packing of ligands and stabilizing the crystal structures. In contrast, 1D-$Cu_2I_2(tpp)_2(pz)$ and 1D-$Cu_2I_2(tpp)_2(4,4'$-bpy) have weaker intermolecular interactions as the ligand aromatic rings stay almost perpendicular to each other. These factors combine to make the double-stranded structures thermally more stable than the single-stranded ones.

To evaluate their suitability for practical lighting applications, compounds **1** and **5** were selected to conduct long-term photo-stability and thermal stability tests. After prolonged heating of the two samples in air and at 150 °C for one month, the IQYs of both samples decreased by less than 10% compared to their initial values (Fig. 5c). A similar long-term photostability test was also conducted, in which the IQYs were measured at selected time intervals upon continuous UV irradiation for one month. Only a 5% loss was observed for the two compounds (Fig. 5c inset). Both compounds retain their crystallinity after these tests as confirmed by the PXRD analysis (Fig. S19, ESI†). In contrast, molecular species 0D-$Cu_2I_2(py)_2$ and single-stranded 1D-$Cu_2I_2(tpp)_2(pz)$ suffer from a nearly 100% drop in their IQYs after heating at 150 °C for only 1 day. Similarly their IQYs reduced by ∼60% and ∼50% at the end of the photostability experiment.

Fabrication of a prototype white LED bulb

A white LED (WLED) bulb was assembled by coating a commercial blue LED chip with compound **5** as the yellow phosphor. A solution of the phosphor and a water soluble polymer binder was prepared in ethanol, and the solution was then applied on a blue LED chip. After drying the phosphor in air for less than 10 minutes, the bulb was ready for use. A photograph of the WLED and blue LED under working conditions is shown in Fig. 5d. The quality of the white light remains unchanged after one month of continuous illumination. After the test, the pure phosphor was isolated by washing the polymer binder containing powder with ethanol. The PL intensity of the isolated yellow phosphor after the test decreased slightly (Fig. S30, ESI†). Both IQYs and EQYs of the phosphor sample were measured before and after the test. Only about a 4.3% loss was observed for IQYs after the test (Table S6†).

Conclusions

A series of multiple-stranded one-dimensional inorganic–organic hybrid materials based on Cu_mI_m molecular clusters ($m = 2, 4, 6$) and benzotriazole derivatives have been synthesized, guided by a rational design strategy and theoretical calculations. These materials exhibit significantly enhanced thermal/photo-stability because they contain strong Cu–N bonds, multiple-stranded connections between the Cu_mI_m core and ligands, and favorable π–π interactions between aromatic ligands. The deliberately selected ligands with low-lying LUMO orbitals are most responsible for the small bandgaps and strong blue-light excitability of the resulting hybrid compounds. The mechanisms of emission in these compounds are dominated by charge transfer from the Cu_mI_m core to the organic ligands, as

examined by temperature dependent photoluminescence and luminescence decay measurements. The emission measurements indicate a strong temperature dependence of intensity and lifetime. Further analysis on the lifetime was carried out by fitting the lifetime curves with two-exponential equations. The results demonstrate that phosphorescence occurs along with thermally activated recombination that is either non-radiative in nature or that proceeds by thermally activated delayed fluorescence. A prototype white light bulb was fabricated by coating a yellow phosphor on a blue LED chip. The emission intensity and quality were well maintained after one month of continuous illumination in air. This study serves as a good example of target-specific approaches to the improvement of properties. The same approach can be applied to form 2D and 3D structures with further enhanced stability.

Conflicts of interest

There are no conflicts to declare.

Acknowledgements

Notes and references

1 X. Huang, J. Li, Y. Zhang and A. Mascarenhas, *J. Am. Chem. Soc.*, 2003, **125**, 7049–7055.

2 D. B. Mitzi, *Adv. Mater.*, 2009, **21**, 3141–3158.

3 C. R. Kagan, D. B. Mitzi and C. D. Dimitrakopoulos, *Science*, 1999, **286**, 945–947.

4 X. Zhang, W. Liu, G. Z. Wei, D. Banerjee, Z. Hu and J. Li, *J. Am. Chem. Soc.*, 2014, **136**, 14230–14236.

5 X. Zhang, M. Hejazi, S. J. Thiagarajan, W. R. Woerner, D. Banerjee, T. J. Emge, W. Xu, S. J. Teat, Q. Gong, A. Safari, R. Yang, J. B. Parise and J. Li, *J. Am. Chem. Soc.*, 2013, **135**, 17401–17407.

6 X. Huang and J. Li, *J. Am. Chem. Soc.*, 2007, **129**, 3157–3162.

7 R. Hoffmann, *Angew. Chem., Int. Ed.*, 2013, **52**, 93–103.

8 R. Peng, M. Li and D. Li, *Coord. Chem. Rev.*, 2010, **254**, 1–18.

9 N. J. Jeon, J. H. Noh, Y. C. Kim, W. S. Yang, S. Ryu and S. I. Seok, *Nat. Mater.*, 2014, **13**, 897.

10 J.-H. Im, I.-H. Jang, N. Pellet, M. Grätzel and N.-G. Park, *Nat. Nanotechnol.*, 2014, **9**, 927–932.

11 D. Liu and T. L. Kelly, *Nat. Photonics*, 2014, **8**, 133–138.

12 M. I. Saidaminov, A. L. Abdelhady, B. Murali, E. Alarousu, V. M. Burlakov, W. Peng, I. Dursun, L. Wang, Y. He, G. Maculan, A. Goriely, T. Wu, O. F. Mohammed and O. M. Bakr, *Nat. Commun.*, 2015, **6**, 7586.

13 D. P. McMeekin, G. Sadoughi, W. Rehman, G. E. Eperon, M. Saliba, M. T. Hörantner, A. Haghighirad, N. Sakai, L. Korte, B. Rech, M. B. Johnston, L. M. Herz and H. J. Snaith, *Science*, 2016, **351**, 151–155.

14 G. E. Eperon, T. Leijtens, K. A. Bush, R. Prasanna, T. Green, J. T.-W. Wang, D. P. McMeekin, G. Volonakis, R. L. Milot, R. May, A. Palmstrom, D. J. Slotcavage, R. A. Belisle, J. B. Patel, E. S. Parrott, R. J. Sutton, W. Ma, F. Moghadam, B. Conings, A. Babayigit, H.-G. Boyen, S. Bent, F. Giustino, L. M. Herz, M. B. Johnston, M. D. McGehee and H. J. Snaith, *Science*, 2016, **354**, 861–865.

15 Z. Yuan, C. Zhou, Y. Tian, Y. Shu, J. Messier, J. C. Wang, L. J. van de Burgt, K. Kountouriotis, Y. Xin, E. Holt, K. Schanze, R. Clark, T. Siegrist and B. Ma, *Nat. Commun.*, 2017, **8**, 14051.

16 Y. Yasuhiro, N. Toru, E. Masaru, W. Atsushi and K. Yoshihiko, *Appl. Phys. Express*, 2014, **7**, 032302.

17 L. Wei, F. Yang and L. Jing, *Adv. Funct. Mater.*, 2018, **28**, 1705593.

18 D. B. Mitzi, C. A. Feild, Z. Schlesinger and R. B. Laibowitz, *J. Solid State Chem.*, 1995, **114**, 159–163.

19 C. Zhang, D. Sun, C. X. Sheng, Y. X. Zhai, K. Mielczarek, A. Zakhidov and Z. V. Vardeny, *Nat. Phys.*, 2015, **11**, 427.

20 C. Dae Sung, K. Yun-Hi and L. Jong-Soo, *Nanotechnology*, 2014, **25**, 035202.

21 N. A. Yelovik, A. V. Mironov, M. A. Bykov, A. N. Kuznetsov, A. V. Grigorieva, Z. Wei, E. V. Dikarev and A. V. Shevelkov, *Inorg. Chem.*, 2016, **55**, 4132–4140.

22 T. R. Amarante, M. M. Antunes, A. A. Valente, F. A. A. Paz, M. Pillinger and I. S. Gonçalves, *Inorg. Chem.*, 2015, **54**, 9690–9703.

23 L. Dou, Y. Yang, J. You, Z. Hong, W.-H. Chang, G. Li and Y. Yang, *Nat. Commun.*, 2014, **5**, 5404.

24 Y. Fang, W. Liu, S. J. Teat, G. Dey, Z. Shen, L. An, D. Yu, L. Wang, D. M. O'Carroll and J. Li, *Adv. Funct. Mater.*, 2017, **27**, 1603444.

25 W. Liu, K. Zhu, S. J. Teat, G. Dey, Z. Shen, L. Wang, D. M. O'Carroll and J. Li, *J. Am. Chem. Soc.*, 2017, **139**, 9281–9290.

26 G. Li, Y. Tian, Y. Zhao and J. Lin, *Chem. Soc. Rev.*, 2015, **44**, 8688–8713.

27 M. Shang, C. Li and J. Lin, *Chem. Soc. Rev.*, 2014, **43**, 1372–1386.

28 W. Liu, Y. Fang, G. Z. Wei, S. J. Teat, K. Xiong, Z. Hu, W. P. Lustig and J. Li, *J. Am. Chem. Soc.*, 2015, **137**, 9400–9408.

29 A. Bril and A. W. de Jager-Veenis, *J. Electrochem. Soc.*, 1976, **123**, 396–398.

30 X. Bai, G. Caputo, Z. Hao, V. Freitas, J. Zhang, R. L. Longo, O. L. Malta, R. A. S. Ferreira and N. Pinna, *Nat. Commun.*, 2014, **5**, 5702.

31 *PLQY Measurement Software U6039-05 Instruction Manual*, Hamamatsu Photonics K.K., Hamamatsu City, Japan, 2012, p. 108.

32 W.-R. Liu, C.-H. Huang, C.-P. Wu, Y.-C. Chiu, Y.-T. Yeh and T.-M. Chen, *J. Mater. Chem.*, 2011, **21**, 6869–6874.

33 G. Paolo, B. Stefano, B. Nicola, C. Matteo, C. Roberto, C. Carlo, C. Davide, L. C. Guido, C. Matteo, D. Ismaila, C. Andrea Dal, G. Stefano de, F. Stefano, F. Guido, G. Ralph, G. Uwe, G. Christos, K. Anton, L. Michele, M.-S. Layla, M. Nicola, M. Francesco, M. Riccardo, P. Stefano, P. Alfredo, P. Lorenzo, S. Carlo, S. Sandro, S. Gabriele, P. S. Ari, S. Alexander, U. Paolo and M. W. Renata, *J. Phys.: Condens. Matter*, 2009, **21**, 395502.

34 J. P. Perdew, M. Ernzerhof and K. Burke, *J. Chem. Phys.*, 1996, **105**, 9982–9985.

35 C. Adamo and V. Barone, *J. Chem. Phys.*, 1999, **110**, 6158–6170.

36 J. Muscat, A. Wander and N. M. Harrison, *Chem. Phys. Lett.*, 2001, **342**, 397–401.

37 D. R. Hamann, M. Schlüter and C. Chiang, *Phys. Rev. Lett.*, 1979, **43**, 1494–1497.

38 X.-J. Yang, H.-X. Li, Z.-L. Xu, H.-Y. Li, Z.-G. Ren and J.-P. Lang, *CrystEngComm*, 2012, **14**, 1641–1652.

39 Y. Zhang, X. He, J. Zhang and P. Feng, *Cryst. Growth Des.*, 2011, **11**, 29–32.

40 R. Czerwieniec, M. J. Leitl, H. H. H. Homeier and H. Yersin, *Coord. Chem. Rev.*, 2016, **325**, 2–28.

41 M. J. Leitl, V. A. Krylova, P. I. Djurovich, M. E. Thompson and H. Yersin, *J. Am. Chem. Soc.*, 2014, **136**, 16032–16038.

42 J. Clark Stewart, D. Segall Matthew, J. Pickard Chris, J. Hasnip Phil, I. J. Probert Matt, K. Refson and C. Payne Mike, *Z. Kristallogr.–Cryst. Mater.*, 2005, **220**, 567.

43 C. L. Raston and A. H. White, *J. Chem. Soc., Dalton Trans.*, 1976, 2153–2156.